



Mid-loaf crisis: Internal breadcrust surfaces in rhyolitic pyroclasts reveal dehydration quenching

Hugh Tuffen¹, Jamie I. Farquharson¹, Fabian B. Wadsworth², Cameron Webb^{1,3}, Jacqueline Owen¹, Jonathan M. Castro⁴, Kim Berlo⁵, C. Ian Schipper⁶ and Katia Wehbe⁷

¹Lancaster Environment Centre, Lancaster University, Lancaster LA1 4YQ, UK

²Department of Earth Sciences, Durham University, Durham DH1 3LE, UK

³Environment Agency, Rotherham S60 1BY, UK

⁴Institute of Geosciences, Johannes Gutenberg Universität, Mainz D-55128, Germany

⁵Department of Earth and Planetary Sciences, McGill University, Montreal, Quebec H3A 0E8, Canada

⁶School of Geography, Environment and Earth Sciences, Victoria University of Wellington, Wellington 6012, New Zealand

⁷B22: MIRIAM, Diamond Light Source Ltd, Oxford OX11 0DE, UK

ABSTRACT

Breadcrust bombs are pyroclasts displaying fractured, dense surfaces enveloping expanded interiors, and are associated with Vulcanian explosions. We document pyroclasts from the 2008–2009 CE eruption of Chaitén (Chile) that are internally as well as externally breadcrusted. The pyroclasts are cut by intersecting micrometer- to millimeter-thick tuffisites with dense glassy walls, which grade into strongly inflated pumiceous material. We find H₂O diffusion gradients proximal to the breadcrusted surfaces, such that H₂O is depleted from far-field magma (0.68 ± 0.04 wt%) into dense, fractured vein walls (0.2–0.3 wt%), indicating a spatial association between H₂O mass transfer within the pyroclast interior and both suppressed vesiculation and breadcrusting. We experimentally confirm that diffusive H₂O depletion suppresses bubble growth at shallow conduit conditions. Therefore, we interpret the breadcrust formation to be induced by H₂O diffusion and the associated rise in viscosity rather than by cooling in the classical breadcrust-formation models. We posit that a “dehydration quench” is important as degassing continues to very low H₂O contents in shallow-conduit magma that continues to vesiculate.

INTRODUCTION

Breadcrust bombs are ballistic pyroclasts ejected explosively during Vulcanian events (e.g., Self et al., 1979) and characterized by dense, cracked, and quenched exteriors that grade into comparatively vesicular interiors (Johnston-Lavis, 1888; Wright et al., 2007). The cracking indicates rheological surface stiffening preceding the cessation of interior expansion, conventionally attributed to relatively rapid thermal quenching of outer surfaces in air or water (Walker, 1969; Fisher and Schmincke, 1984) while slower-cooled interiors undergo decompression-triggered, post-fragmentation vesiculation (e.g., Wright et al., 2007). Bomb textures and volatile concentrations record pre-blast conduit conditions (Wright et al., 2007; Giachetti et al., 2010): to vesiculate during bomb ejection, magma must exceed an H₂O supersaturation threshold, typically in the range 0.4–0.9 wt% (Hoblitt and Harmon, 1993; Wright

et al., 2007; Bain et al., 2019). However, recently identified pyroclast breadcrust textures (Quane and Andrews, 2020) suggest that breadcrust formation may commonly be more complex than described by this general model.

Recent rhyolitic eruptions at Chaitén and Cordón Caulle (Chile) involved hybrid explosive-effusive activity from a common vent above a compacting lava plug (Pallister et al., 2013; Schipper et al., 2013). Explosive upper-conduit fracturing and tuffisite formation facilitated transient outgassing (Castro et al., 2012, 2014; Saubin et al., 2016; Paisley et al., 2019; Schipper et al., 2021), allowing high-flux effusion of dense rhyolite (e.g., Wadsworth et al., 2020), until welding and healing rendered them impermeable (Farquharson et al., 2017; Heap et al., 2019; Wadsworth et al., 2021). Characterization of tuffisite veins is yet to be integrated into studies of breadcrust bombs, despite common causes (gas overpressure), process implica-

tions (explosive plug disruption), and resultant products (partially vesiculated, vein-hosting, glassy pyroclasts). We document pumiceous, tuffisite-bearing rhyolitic pyroclasts from the 2008–2009 Chaitén eruption, which exhibit an interconnected network of internal and external breadcrusted surfaces.

GEOLOGICAL CONTEXT

The 2008–2009 eruption of Chaitén (~42°S; Chilean Patagonia; Fig. 1) began on 1 May 2008 following 24 h of seismicity (Castro and Dingwell, 2009) with dike-driven ascent of near-aphyric, high-silica rhyolite from a 5–10-km-deep source region (Pallister et al., 2013). Activity spanned phases 1 (explosive, 10 d), 2 (hybrid activity, 20 d), and 3 (effusive lava emplacement, several months). Column-collapse pyroclastic density currents (PDCs) were emplaced within the caldera late in phase 1; phase 2 involved eruption of rhyolitic lava domes and coulées with synchronous, repeated Vulcanian explosions and intermittent PDC-producing plumes (Pallister et al., 2013), with deposits emplaced on the caldera floor (Fig. 1).

TEXTURAL DESCRIPTION

We studied an irregular pyroclast (15 × 25 × 20 cm) (Fig. 2) that is typical of many deposits emplaced during the latter part of phase 1, including bombs and bomb fragments. The outer surface of the pyroclast is variably coated with centimetric red- or brown-colored plates of sintered fine-grained clastic material, delineated by polygonal fractures in jigsaw-fit organization (Figs. 2A, 2B, 2E, and 2F) commonly interpreted as unambiguous evidence of

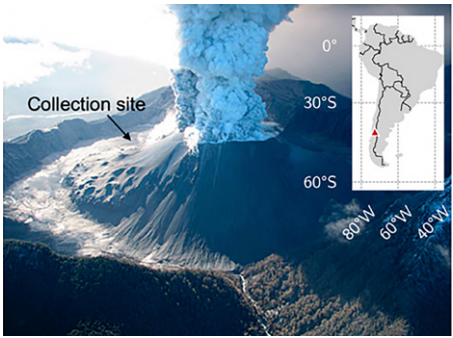


Figure 1. Hybrid explosive-effusive activity at Chaitén volcano (Chile), photographed on 26 May 2008 (J.N. Marso, U.S. Geological Survey). Arrow indicates the sampling location. Inset: Location map of Chaitén (triangle).

cooling- and vesiculation-induced breadcrusting. These surface textures can be tracked into the pyroclast interior (Figs. 2C and 2D), which is characterized by a network of prominent millimeter-thick tuffisites. Viewed in cross section,

the characteristic breadcrust surface texture and the internal tuffisites are clearly manifestations of the same structures. Cross-cutting tuffisites (Fig. 2G) indicate two separate fracture events (early and late stage).

Late-stage tuffisites comprise curviplanar veins filled by red-brown sintered fragments (as locally observed on the outer clast surface) flanked by ~10-μm-thick, dense obsidian selvages normal to the tuffosite plane. These dense walls grade into pumiceous material that makes up the majority of the clast interior. Early-stage tuffisites are cut by their late-stage counterparts (Fig. 2G), and themselves cut through variably dense flow bands (Fig. 2C). Early-stage tuffisites exhibit thick glassy walls (~2 mm; Fig. 2G). The incipiently sintered early-stage tuffosite fill consists of angular to subrounded, fine-grained (~1–20 μm) glassy clasts (Fig. 2H). The network of cross-cutting veins delineates discrete angular domains of high-vesicularity material (Figs. 2C and 2G). The clastic veneer that coats the pyroclast surface and fills late-stage tuffisites

is cut by tensile fractures (Figs. 2E and 2F)—manifest as variable segmentation in cross section (Fig. 2G)—while the underlying pumice has flowed viscously into the resultant voids (Figs. 2F and 2H), similar to textures observed in mesoscale boudinage structures in vesicular rhyolite domes (e.g., Panum Crater dome, California, USA; Castro and Cashman, 1999). Dense tuffosite walls and clastic fill therefore signify distinct rheological responses to the viscous, vesicular material.

WATER MOBILITY AND DEGASSING

We used benchtop and synchrotron-source Fourier-transform infrared spectroscopy (FTIR and sFTIR, respectively) to quantify dissolved H₂O concentrations in transects normal to an early-stage tuffosite (Figs. 3A–3C). H₂O content is typically lower within the tuffosite than in the surrounding pyroclast (mean value of 0.31 wt% H₂O relative to ~0.68 wt% in the far field; Fig. 3A). All transects exhibit systematic H₂O decreases from far-field values of ~0.68 ± 0.04 wt% toward the tuffosite wall (Figs. 3A and 3C). Minimum measured values at the wall were 0.16 wt% for sFTIR (Fig. 3A) and 0.28 wt% for FTIR (Fig. 3C). All transects (Fig. 3) represent atypical diffusion gradients inasmuch as vesiculation has overprinted the diffusion process. The approximate pyroclast center porosity φ is 0.6, and this post-fragmentation vesiculation has modified measured H₂O concentrations via mass transfer into bubbles. Toward the dense obsidian edge, vesiculation has also diluted the spatial coordinates in the observed H₂O gradient. In the Supplemental Material¹, we provide a quantitative correction for these effects in order to rectify the diffusion gradient for further analysis (Fig. 3C). In all transects, the measured H₂O depletion occurs over a length scale of $L \sim 300 \mu\text{m}$, indicating diffusive outgassing into the vein. We defined the diffusion time scale as $\lambda_D = L^2/(4D)$, with diffusivity $D \approx 1.3 \times 10^{-12} \text{ m}^2 \text{ s}^{-1}$ (Zhang and Ni, 2010) for 825°C. The diffusion time scale required to produce the observed gradient length scales is $\lambda_D = 4.81 \text{ h}$. Similarly, we applied a simplified one-dimensional diffusion model (Crank, 1979),

$$c(x) = c_b + (c_0 - c_b) \operatorname{erfc} \left[x / \left(2\sqrt{Dt_D} \right) \right], \quad (1)$$

where erfc is the complementary error function and c_b is the observed value of H₂O concentration c at the wall. Using a least-squares minimization

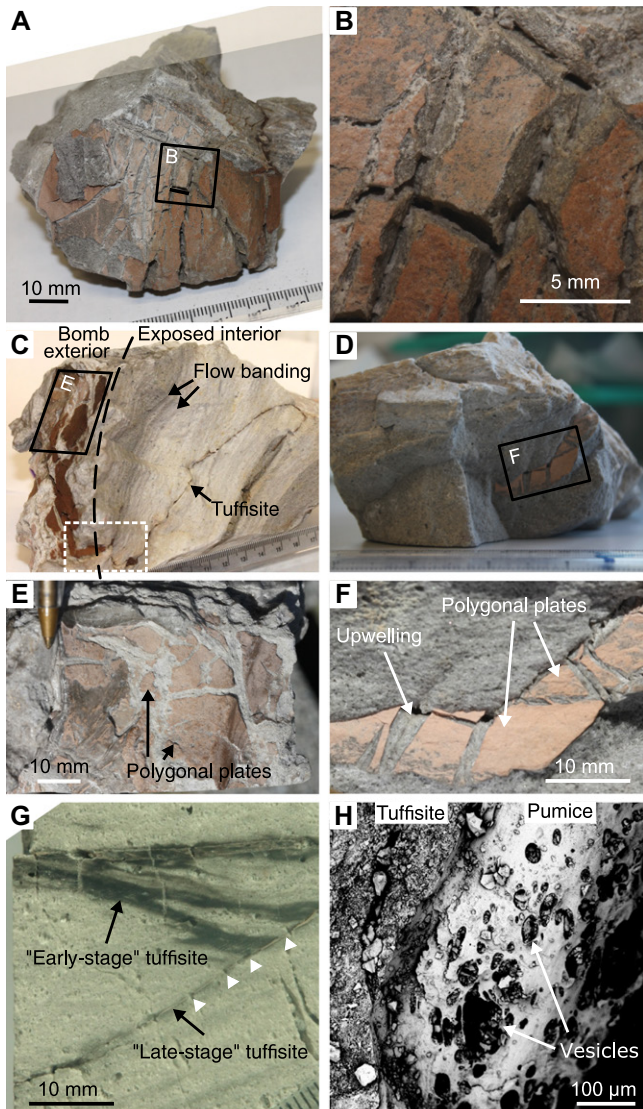


Figure 2. Textures within the Chaitén volcano (Chile) pyroclast sample. (A) Clast overview, showing red-brown, fractured plates of clastic material on the surface. (B) Detail of the surface breadcrust texture. (C) Overview: red-brown, fractured plates of clastic material on the surface, connected to tuffosite that cross-cuts flow bands in the clast interior (dashed box). Scale is in centimeters. (D) Overview: tuffosite partially exposed at the clast surface. (E) Detail of C, showing centimeter-scale polygonal plates of breadcrust on the surface that comprise the clastic red veneer overlying dense gray glass. (F) Exposed tuffosite, showing separation of sintered tuffosite, indicating a tensile linear strain of as much as ~0.25. (G) Cross section showing an early-stage tuffosite with ~100-μm-thick dense walls, cross-cut by a late-stage vein. White triangles mark late-stage tuffosite segmentation. (H) Scanning electron microscope image of late-stage tuffosite: poorly sintered ash adhering to the glassy surface, adjacent to a vesiculated pumiceous texture (porosity shown as black).

¹Supplemental Material. The corrections applied to the as-measured diffusion data, accounting for the post-diffusion volumetric expansion of the clast. Please visit <https://doi.org/10.1130/GEOLOGY.2019.19879786> to access the supplemental material, and contact editing@geosociety.org with any questions.

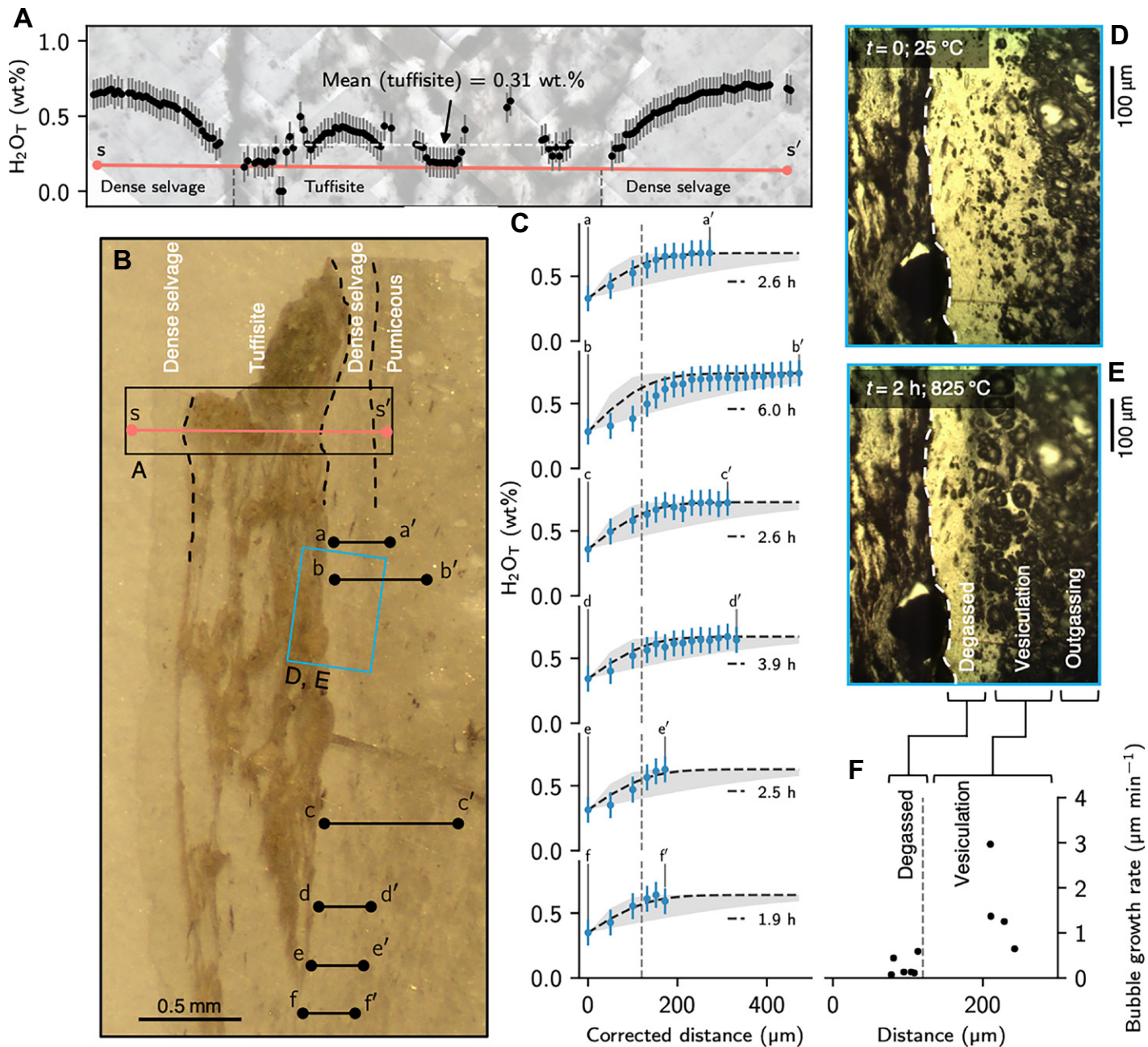


Figure 3. (A) Synchrotron-source Fourier-transform infrared spectroscopy (sFTIR) transect s-s' crossing tuffsite (see B), with measured weight-percent H_2O_T (T —total dissolved H_2O) relative to the transect position. Error bars indicate 10% error margin. (B) Sample wafer, indicating location of benchtop Fourier-transform infrared spectroscopy (FTIR) and sFTIR transects (s-s' and a-a' to f-f') and the wafer used in the hot-stage experiment (blue box). (C) FTIR-derived H_2O_T as a function of corrected distance along the transect from the tuffsite (see B, and the Supplemental Material [see footnote 1]) for each transect a-a' to f-f'. Error bars indicate 10% error margin. Curved black dashed line shows the best-fit diffusion profile and corresponding diffusion time scale. Gray shaded region shows the envelope for time scales of 0.5–20 h. (D) Pre-heating sample wafer (time $t = 0$). White dashed line indicates the tuffsite wall. (E) Post-heating sample wafer ($t = 2$ h; 825°C). (F) Bubble growth rate as a function of initial vesicle distance from the tuffsite wall. Porosity threshold (see the Supplemental Material) indicated by the vertical dashed line in C and F.

to the observed $c(x)$ profile, we computed the time t_D over which diffusion occurred. We find $t_D = 1.9\text{--}6.0$ h (Fig. 3C), consistent with other estimates for Chaitén tuffsites (Castro et al., 2012; Berlo et al., 2013; Saubin et al., 2016; Heap et al., 2019) and with the scaled timescale λ_D . Assuming far-field H_2O concentration is the pre-ejection solubility value, solubility modeling (Newman and Lowenstern, 2002) predicts

equilibration at 4 MPa pressure, a magmatic depth of 170 m (similar to pyroclast depth estimates from Castro et al. [2014]).

EXPERIMENTAL VESICULATION

We heated a polished wafer (~ 112 μm thick) from the early-stage tuffsite margin at $200^\circ\text{C min}^{-1}$ and ambient pressure to 825°C in a Linkam TS1500 heated stage attached to

a Zeiss AxioScope 1 microscope with Pixelink camera. For full methods, see Browning et al. (2020). Images were acquired to characterize the rate and spatial distribution of vesicle nucleation and growth over 2 h (Figs. 3D–3F). H_2O concentration across the transect from dense glass to pumiceous material was also measured prior to the experiment. As in other transects (Figs. 3A and 3C), the pre-experiment sample exhibited

increasing H₂O with distance from the tuffsite wall. Vesiculation was entirely suppressed in the dense glassy zone with H₂O < 0.5 wt% (Fig. 3F), with negligible additional vesiculation in the pumiceous zone (~110 μm from the wall), indicating that the pumiceous zone was above the percolation threshold—permeable outgassing occurred (Vasseur et al., 2020). However, the medial zone was sufficiently saturated to allow exsolution and bubble nucleation, manifest in calculated bubble growth rates of ≤3.0 μm min⁻¹, highlighting textural predisposition to thermal vesiculation.

POST-TUFFSISITE PYROCLAST VESICULATION AND COOLING

The pyroclast exhibits the characteristic—typical of ballistic ejecta—of highest vesicularity at its center. This reflects slower cooling and extended post-fragmentation vesiculation within the clast relative to the surface (e.g., Wright et al., 2007; Giachetti et al., 2010). Pyroclast cooling time scales can be scaled as $\lambda_T = R^2/(4D_T)$, where D_T is thermal diffusivity ($\approx 6 \times 10^{-7}$; Bagdassarov and Dingwell, 1994) and R is the pyroclast radius. Estimating $R = 0.15$ m, we find $\lambda_T = 2.6$ h, which

represents the time available for vesiculation spanning pyroclast decompression, ejection, and quenching. We note that $\lambda_T \approx \lambda_D$, with the lower-bound $\lambda_D < \lambda_T$, demonstrating that the diffusive mass transfer of H₂O can occur during the thermal lifetime of the clast. This is consistent with the observation that vesiculation has driven fracturing (Fig. 2F).

Breadcrust features of the late-stage tuffsite (Figs. 2F and 2G) are characterized by displacements between fragments of crust. We argue that the late-stage vein and its walls were more viscous than the far-field melt due to relative volatile depletion, embrittling the magma adjacent to the vein margins. Although the tuffsite fill is clastic, it has undergone some sintering and would have been capable of cohesive viscous deformation (e.g., Tuffen and Dingwell, 2005). A range of plausible viscosities η were calculated (Giordano et al., 2008) using the composition of Chaitén melt (Castro and Dingwell, 2009) and the range of measured H₂O concentrations within the sample (Fig. 4A). Assuming the total time for bubble growth $t_B = 60$ s is the time available for vesiculation-derived deformation (Browning et al., 2020), and linear strain γ of 0.25 estimated from the fragment offsets along

planar portions of the vein (Fig. 2F), we estimate a bulk linear strain rate $\dot{\gamma} = \gamma/t_B = 0.0042$ s⁻¹. Using this $\dot{\gamma}$, we estimate a threshold viscosity for brittle melt failure: $\eta_C = \sigma_C/\dot{\gamma}_C$, where σ_C is the threshold stress for failure ($\sigma_C = 10^8$ Pa; Webb and Dingwell, 1990; Wadsworth et al., 2018). We find that $\eta_C = 2.38 \times 10^{10}$ Pa·s. In Figure 4, we show that a viscous deformation response to vesiculation-driven strain is expected for the non-H₂O-depleted far-field regions at ejection temperatures of >750°C—due to their lower viscosity—allowing clast expansion. By contrast, neighboring volatile-depleted, higher-viscosity melt would fail mechanically, despite being at the same temperature, underpinning our model for degassing-driven internal breadcrusting.

CONCEPTUAL MODEL AND CONCLUSIONS

We interpret the pyroclast sample as recording at least two in-conduit fracture events, periods of sintering, and vesiculation and ejection-related decompression and cooling. We infer the following sequence (Fig. 4B): (0) a homogenous, dense aliquot of magma was resident at ~170 m depth; (1) a fracture event occurred, forging pathways for gas and/or ash flow through the magma; (2) H₂O depletion occurred over the lifespan of these fractures, leaving volatile-poor—rheologically stiffer—magma adjacent to the fracture walls; (3) fracture closure was accompanied or driven by partial sintering of the fine-grained material inside—at this stage or contemporaneous with stage 4, a second generation of fractures was also created (Fig. 2E); (4) decompression-driven vesiculation occurred with the magma adjacent to the former outgassing pathways remaining non-vesicular due to vesiculation suppression; and (5) a brittle response in the mechanically coupled volatile-poor selvages and incipiently sintered tuffsite fill, which resulted in breadcrusting both within the pyroclast interior and on its outer surface. Pyroclast ejection occurred along with stage 4 or in an explosion shortly afterward (Fig. 4C). Stages 0–5 all occurred within the thermal lifetime of the pyroclast, pre- and syn-ejection. Both volatile depletion toward the vein and preferential vesiculation distal from tuffsites in this pyroclast led to rheological stiffening associated with degassing that depended primarily on chemical diffusion: an isothermal degassing quench (Ryan et al., 2015) rather than a thermal quench. To date, breadcrust textures in volcanic deposits have been interpreted as unambiguous evidence of a thermal quenching process. Our alternative mechanism for breadcrust formation—a chemorheological, rather than thermo-rheological, process—suggests that similar textures recorded in volcanic deposits worldwide may require reanalysis and reinterpretation. Such textures

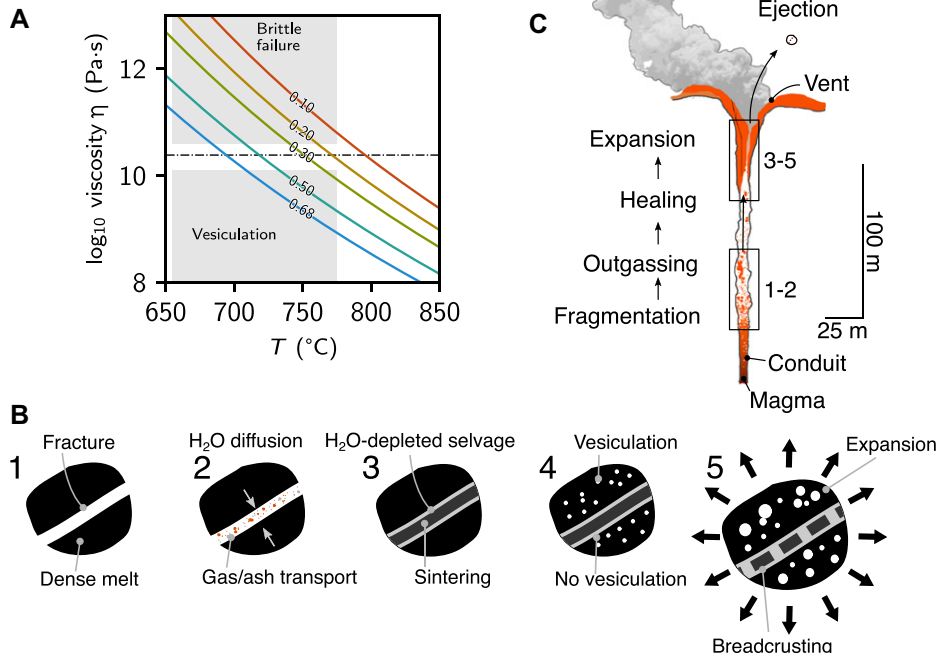


Figure 4. (A) Viscosity η as function of temperature T (Giordano et al., 2008), shown for water concentrations of 0.68–0.1 wt% and Chaitén volcano (Chile) glass melt composition. Approximate brittle failure and vesiculation regimes are highlighted. Dashed line indicates $\sigma_C/\dot{\gamma}_C$ (brittle failure threshold; σ_C is threshold stress for failure [10^8 Pa] and $\dot{\gamma}_C$ is critical strain rate). (B) Schematic of the dehydration quench mechanism. (1) Fracture is created within a dense, avesicular magma aliquot. (2) Fracture is exploited as a gas and/or ash venting pathway; H₂O diffuses from melt into the fracture. (3) Diffusion leaves an H₂O-depleted selvage; sintering of hot ash particles effectively seals the fracture. (4) Far-field magma vesiculates, but the fracture-adjacent H₂O-poor regions do not. (5) Bubble-driven bomb expansion elicits viscous deformation in H₂O-rich melt zones (i.e., low viscosity: A), but H₂O-depleted regions undergo brittle response. (C) Contextual cartoon of in-conduit processes described in B, shallowing from stages 1 to 5.

may occur in explosively ejected fragments of conduit plugs, where they have previously been uniquely interpreted as thermal quench features (i.e., classic breadcrust bombs), and also within silicic lavas, where relatively dense layers—e.g., tuffisites—have been segmented by heterogeneous vesiculation (Castro and Cashman, 1999; Andrews et al., 2021).

ACKNOWLEDGMENTS

We are grateful for financial support from the Royal Society (grant URF UF140716, to support H. Tuffen and J. Farquharson), the EC-FP7 Vuelco project (F. Wadsworth), and the AXA Research Fund (J. Owen). N. La Penna and R. Wilbraham assisted in the field and with scanning electron microscope imaging. We wish to acknowledge Amelia Bain, Benjamin Andrews, and Steve Quane for insightful and constructive reviews. We thank Diamond Light Source for access to the MIRIAM beamline B22 that contributed to the results presented here.

REFERENCES CITED

- Andrews, G.D.M., Kenderes, S.M., Whittington, A.G., Ison, S.L., Brown, S.R., Pettus, H.D., Cole, B.G., and Gokey, K.J., 2021, The fold illusion: The origins and implications of ogives on silicic lavas: *Earth and Planetary Science Letters*, v. 553, 116643, <https://doi.org/10.1016/j.epsl.2020.116643>.
- Bagdassarov, N., and Dingwell, D., 1994, Thermal properties of vesicular rhyolite: *Journal of Volcanology and Geothermal Research*, v. 60, p. 179–191, [https://doi.org/10.1016/0377-0273\(94\)90067-1](https://doi.org/10.1016/0377-0273(94)90067-1).
- Bain, A.A., Calder, E.S., Cortés, J.A., Cortés, G.P., and Loughlin, S.C., 2019, Textural and geochemical constraints on andesitic plug emplacement prior to the 2004–2010 vulcanian explosions at Galeras volcano, Colombia: *Bulletin of Volcanology*, v. 81, 1, <https://doi.org/10.1007/s00445-018-1260-y>.
- Berlo, K., Tuffen, H., Smith, V.C., Castro, J.M., Pyle, D.M., Mather, T.A., and Geraki, K., 2013, Element variations in rhyolitic magma resulting from gas transport: *Geochimica et Cosmochimica Acta*, v. 121, p. 436–451, <https://doi.org/10.1016/j.gca.2013.07.032>.
- Browning, J., Tuffen, H., James, M.R., Owen, J., Castro, J.M., Halliwell, S., and Wehbe, K., 2020, Post-fragmentation vesiculation timescales in hydrous rhyolitic bombs from Chaitén volcano: *Journal of South American Earth Sciences*, v. 104, 102807, <https://doi.org/10.1016/j.jsames.2020.102807>.
- Castro, J., and Cashman, K.V., 1999, Constraints on rheology of obsidian lavas based on mesoscopic folds: *Journal of Structural Geology*, v. 21, p. 807–819, [https://doi.org/10.1016/S0191-8141\(99\)00070-X](https://doi.org/10.1016/S0191-8141(99)00070-X).
- Castro, J.M., and Dingwell, D.B., 2009, Rapid ascent of rhyolitic magma at Chaitén volcano, Chile: *Nature*, v. 461, p. 780–783, <https://doi.org/10.1038/nature08458>.
- Castro, J.M., Bindeman, I.N., Tuffen, H., and Schipper, C.I., 2014, Explosive origin of silicic lava: Textural and $\delta\text{D}-\text{H}_2\text{O}$ evidence for pyroclastic degassing during rhyolite effusion: *Earth and Planetary Science Letters*, v. 405, p. 52–61, <https://doi.org/10.1016/j.epsl.2014.08.012>.
- Castro, J.M., Cordonnier, B., Tuffen, H., Tobin, M.J., Puskar, L., Martin, M.C., and Bechtel, H.A., 2012, The role of melt-fracture degassing in defusing explosive rhyolite eruptions at volcán Chaitén: *Earth and Planetary Science Letters*, v. 333–334, p. 63–69, <https://doi.org/10.1016/j.epsl.2012.04.024>.
- Crank, J., 1979, *The Mathematics of Diffusion* (2nd Edition): Oxford, UK, Clarendon Press, 428 p.
- Farquharson, J.I., Wadsworth, F.B., Heap, M.J., and Baud, P., 2017, Time-dependent permeability evolution in compacting volcanic fracture systems and implications for gas overpressure: *Journal of Volcanology and Geothermal Research*, v. 339, p. 81–97, <https://doi.org/10.1016/j.jvolgeores.2017.04.025>.
- Fisher, R.V., and Schmincke, H.-U., 1984, Pyroclastic rocks and tectonic environment, in Fisher, R.V., and Schmincke, H.-U., eds., *Pyroclastic Rocks*: Berlin, Heidelberg, Springer, p. 383–409, https://doi.org/10.1007/978-3-642-74864-6_14.
- Giachetti, T., Druitt, T.H., Burgisser, A., Arbaret, L., and Galven, C., 2010, Bubble nucleation, growth and coalescence during the 1997 Vulcanian explosions of Soufrière Hills Volcano, Montserrat: *Journal of Volcanology and Geothermal Research*, v. 193, p. 215–231, <https://doi.org/10.1016/j.jvolgeores.2010.04.001>.
- Giordano, D., Russell, J.K., and Dingwell, D.B., 2008, Viscosity of magmatic liquids: A model: *Earth and Planetary Science Letters*, v. 271, p. 123–134, <https://doi.org/10.1016/j.epsl.2008.03.038>.
- Heap, M.J., Tuffen, H., Wadsworth, F.B., Reuschlé, T., Castro, J.M., and Schipper, C.I., 2019, The permeability evolution of tuffisites and implications for outgassing through dense rhyolitic magma: *Journal of Geophysical Research: Solid Earth*, v. 124, p. 8281–8299, <https://doi.org/10.1029/2018JB017035>.
- Hoblitt, R.P., and Harmon, R.S., 1993, Bimodal density distribution of cryptodome dacite from the 1980 eruption of Mount St. Helens, Washington: *Bulletin of Volcanology*, v. 55, p. 421–437, <https://doi.org/10.1007/BF00302002>.
- Johnston-Lavis, H.J., 1888, Further notes on the late eruption at Vulcano Island: *Nature*, v. 39, p. 109–111, <https://doi.org/10.1038/039109a0>.
- Newman, S., and Lowenstern, J.B., 2002, Volatile-Calc: A silicate melt- $\text{H}_2\text{O}-\text{CO}_2$ solution model written in Visual Basic for Excel: *Computers & Geosciences*, v. 28, p. 597–604, [https://doi.org/10.1016/S0098-3009\(01\)00081-4](https://doi.org/10.1016/S0098-3009(01)00081-4).
- Paisley, R., Berlo, K., Whattam, J., Schipper, C.I., and Tuffen, H., 2019, Degassing-induced chemical heterogeneity at the 2011–2012 Cordón Caulle eruption: *Volcanica*, v. 2, p. 211–237, <https://doi.org/10.30909/vol.02.02.211237>.
- Pallister, J.S., Diefenbach, A.K., Burton, W.C., Muñoz, J., Griswold, J.P., Lara, L.E., Lowenstern, J.B., and Valenzuela, C.E., 2013, The Chaitén rhyolite lava dome: Eruption sequence, lava dome volumes, rapid effusion rates and source of the rhyolite magma: *Andean Geology*, v. 40, p. 277–294, <https://doi.org/10.5027/andgeoV40n2-a06>.
- Quane, S.L., and Andrews, B.J., 2020, Breadcrust bubbles: Ash particles recording post-fragmentation brittle-ductile deformation: *Geology*, v. 48, p. 1205–1209, <https://doi.org/10.1130/G47811.1>.
- Ryan, A.G., Russell, J.K., Nichols, A.R.L., Hess, K.-U., and Porritt, L.A., 2015, Experiments and models on H_2O retrograde solubility in volcanic systems: *American Mineralogist*, v. 100, p. 774–786, <https://doi.org/10.2138/am-2015-5030>.
- Saibin, E., Tuffen, H., Gurioli, L., Owen, J., Castro, J.M., Berlo, K., McGowan, E.M., Schipper, C.I., and Wehbe, K., 2016, Conduit dynamics in transitional rhyolitic activity recorded by tuffsite vein textures from the 2008–2009 Chaitén eruption: *Frontiers of Earth Science*, v. 4, 59, <https://doi.org/10.3389/feart.2016.00059>.
- Schipper, C.I., Castro, J.M., Tuffen, H., James, M.R., and How, P., 2013, Shallow vent architecture during hybrid explosive–effusive activity at Cordón Caulle (Chile, 2011–12): Evidence from direct observations and pyroclast textures: *Journal of Volcanology and Geothermal Research*, v. 262, p. 25–37, <https://doi.org/10.1016/j.jvolgeores.2013.06.005>.
- Schipper, C.I., et al., 2021, Silicic conduits as supersized tuffisites: Clastogenic influences on shifting eruption styles at Cordón Caulle volcano (Chile): *Bulletin of Volcanology*, v. 83, 11, <https://doi.org/10.1007/s00445-020-01432-1>.
- Self, S., Wilson, L., and Nairn, I.A., 1979, Vulcanian eruption mechanisms: *Nature*, v. 277, p. 440–443, <https://doi.org/10.1038/277440a0>.
- Tuffen, H., and Dingwell, D., 2005, Fault textures in volcanic conduits: Evidence for seismic trigger mechanisms during silicic eruptions: *Bulletin of Volcanology*, v. 67, p. 370–387, <https://doi.org/10.1007/s00445-004-0383-5>.
- Vasseur, J., Wadsworth, F.B., and Dingwell, D.B., 2020, Permeability of polydisperse magma foam: *Geology*, v. 48, p. 536–540, <https://doi.org/10.1130/G47094.1>.
- Wadsworth, F.B., Witcher, T., Vossen, C.E.J., Hess, K.-U., Unwin, H.E., Scheu, B., Castro, J.M., and Dingwell, D.B., 2018, Combined effusive-explosive silicic volcanism straddles the multiphase viscous-to-brittle transition: *Nature Communications*, v. 9, 4696, <https://doi.org/10.1038/s41467-018-07187-w>.
- Wadsworth, F.B., Llewellyn, E.W., Vasseur, J., Gardner, J.E., and Tuffen, H., 2020, Explosive–effusive volcanic eruption transitions caused by sintering: *Science Advances*, v. 6, eaba7940, <https://doi.org/10.1126/sciadv.aba7940>.
- Wadsworth, F.B., et al., 2021, A model for permeability evolution during volcanic welding: *Journal of Volcanology and Geothermal Research*, v. 409, 107118, <https://doi.org/10.1016/j.jvolgeores.2020.107118>.
- Walker, G.P.L., 1969, The breaking of magma: *Geological Magazine*, v. 106, p. 166–173, <https://doi.org/10.1017/S0016756800051979>.
- Webb, S.L., and Dingwell, D.B., 1990, Non-Newtonian rheology of igneous melts at high stresses and strain rates: Experimental results for rhyolite, andesite, basalt, and nepheline: *Journal of Geophysical Research*, v. 95, p. 15,695–15,701, <https://doi.org/10.1029/JB095iB10p15695>.
- Wright, H.M.N., Cashman, K.V., Rosi, M., and Cioni, R., 2007, Breadcrust bombs as indicators of Vulcanian eruption dynamics at Guagua Pichincha volcano, Ecuador: *Bulletin of Volcanology*, v. 69, p. 281–300, <https://doi.org/10.1007/s00445-006-0073-6>.
- Zhang, Y.X., and Ni, H.W., 2010, Diffusion of H, C, and O components in silicate melts: *Reviews in Mineralogy and Geochemistry*, v. 72, p. 171–225, <https://doi.org/10.2138/rmg.2010.72.5>.

Printed in USA